SMF-VO: Direct Ego-Motion Estimation via Sparse Motion Fields

Sangheon Yang¹, Yeongin Yoon², Hong Mo Jung², and Jongwoo Lim*²

Abstract—Traditional Visual Odometry (VO) and Visual-Inertial Odometry (VIO) methods rely on a "pose-centric" paradigm, which computes absolute camera poses from the local map thus requires large-scale landmark maintenance and continuous map optimization. This approach is computationally expensive, limiting their real-time performance on resource-constrained devices.

To overcome these limitations, we introduce Sparse Motion-Field Visual Odometry (SMF-VO), a lightweight, "motion-centric" framework. Our approach directly estimates instantaneous linear and angular velocity from sparse optical flow, bypassing the need for explicit pose estimation or expensive landmark tracking. We also employed a generalized 3D ray-based motion field formulation that works accurately with various camera models, including wide-field-of-view lenses.

SMF-VO demonstrates superior efficiency and competitive accuracy on benchmark datasets, achieving over 100 FPS on a Raspberry Pi 5 using only a CPU. Our work establishes a scalable and efficient alternative to conventional methods, making it highly suitable for mobile robotics and wearable devices.

I. INTRODUCTION

Visual Odometry (VO) is a fundamental technique for estimating camera motion from visual input and is widely used in robotics, augmented/virtual reality (AR/VR), and autonomous navigation. By analyzing sequential images captured from a monocular, stereo, or RGB-D camera, it estimates the ego-motion of the camera. Despite substantial progress in accuracy and robustness, conventional VO systems still have several limitations, including heavy computational overhead and sensitivity to environmental changes such as lighting variations and dynamic objects.

The main reason for the computational overhead is that traditional feature-based VO algorithms follow the "pose-centric" paradigm, which requires explicit camera pose estimation (P3P or PnP) based on the local map. Since pose accuracy relies critically on map quality, this process requires tracking a large number of accumulated 3D landmarks over multiple keyframes and performing local bundle adjustment to keep the local map accurate, leading to high computational costs and makes real-time operation challenging on resource-constrained platforms.

Visual-inertial odometry (VIO) incorporates inertial measurements to improve reliability in visually degraded conditions. However, this integration introduces new challenges, including multi-sensor calibration, pose drift due to IMU

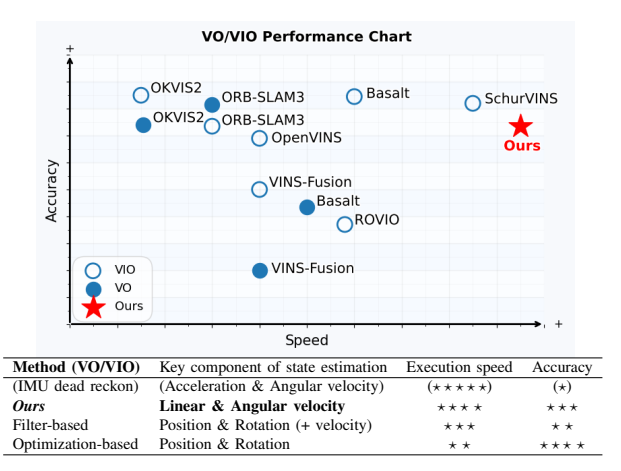


Fig. 1: An overall comparison of the accuracy and speed of VO and VIO algorithms. Our algorithm directly estimates camera motion from the visual motion field. Thus, it runs much faster than conventional VO algorithms without sacrificing accuracy.

bias, and increased algorithmic complexity. Additionally, pose-centric VIO frameworks inherit the computational burdens of VO on landmark tracking and continuous optimization.

To address these challenges, we introduce Sparse Motion-Field Visual Odometry (SMF-VO), a lightweight, high-speed framework that directly estimates ego-motion from motion field equations. Our novel "motion-centric" approach overcomes the limitations of traditional VO and VIO methods by directly calculating the camera's instantaneous linear and angular velocity from sparse optical flow. This method eliminates the need for explicit pose estimation, such as P3P, and the computationally expensive multi-frame optimization required for large-scale landmark maintenance. SMF-VO instead solves a compact per-frame optimization problem using only sparse keypoints in each frame, making it highly efficient for real-time deployment on low-power embedded devices.

Building upon the classical motion field, we employ a generalized 3D ray-based formulation by representing image points as normalized rays. This approach removes the limitations of conventional 2D pixel-based, pinhole-model equations, allowing the resulting SMF-VO framework to accommodate any camera model. This is crucial for handling cameras with varied fields of view and nonlinear projection, like fisheye lenses in robotics.

Through extensive experimentation with various benchmark datasets, including EuRoC, KITTI, and TUM-VI, we

^{*}Corresponding Author

¹Department of Artificial Intelligence, Hanyang University, Seoul, Korea. philippine96@hanyang.ac.kr

²Department of Mechanical Engineering, Seoul National University, Seoul, Korea {yoonyi2017;jjhm2910;jongwoo.lim}@snu.ac.kr

All authors are with the Robot Vision Lab, Seoul National University.

demonstrate that SMF-VO is significantly more computationally efficient than conventional VO methods while maintaining comparable accuracy. The system achieves over 100 frames per second (FPS) on a Raspberry Pi 5 using only a quad-core 2.4 GHz CPU. By pioneering a motion-centric ego-motion estimation paradigm, SMF-VO provides a scalable and efficient alternative to conventional VO, making it a strong candidate for practical, real-life applications in mobile robotics, AR/VR, and wearable devices.

Our work introduces SMF-VO, a novel visual odometry framework that offers three key features.

- A New Motion-Centric Paradigm: We developed a
 new visual odometry approach that directly estimates
 camera ego-motion as linear and angular velocity, instead of using traditional position-based methods. This
 allows for high-efficiency real-time performance without sacrificing accuracy.
- Generalizable Camera Support: We achieve camera model generalizability by employing a generalized 3D ray-based motion field formulation. This existing concept, when applied to our framework, works accurately with various models, including wide field-of-view systems like fisheye lenses, overcoming the limitations of traditional pinhole-only 2D methods.
- Superior Real-World Performance: We validated our system on standard datasets such as EuRoC, KITTI, and TUM-VI. Our algorithm achieved over 100 FPS on a Raspberry Pi 5 using only a CPU, demonstrating its superior efficiency and robustness. This proves its suitability for real-time applications on resourceconstrained devices.

II. RELATED WORKS

Visual and Visual Inertial Odometry. Traditional Visual Odometry (VO) methods can be categorized into featurebased and direct approaches. Feature-based methods [1]-[4] track or match sparse keypoints across frames and use geometric constraints for motion estimation. These methods are effective in well-textured environments, but suffer from unreliable feature correspondences in low-texture or dynamic scenes. Stereo VO [5], [6] incorporates depth information to compute metric motion without scale drift, but remains sensitive to illumination changes and occlusions. Direct methods [7]–[9] estimate motion by minimizing photometric error over pixel intensities rather than relying on feature correspondences. While effective in textureless environments, they are computationally expensive and highly sensitive to lighting variations and motion blur. Optimization-based approaches, such as Bundle Adjustment (BA) and Factor Graph-based SLAM [10], [11], further refine motion estimates but impose a high computational burden, limiting their real-time feasibility on embedded systems. VIO methods integrate an IMU with a camera to enhance robustness in visually degraded environments. Filtering-based methods such as MSCKF [12], ROVIO [13], and SchurVINS [14] use recursive filtering to propagate state estimates, while optimization-based methods such as VINS-Mono [15], Basalt [16], and OKVIS2 [17]

employ non-linear optimization for improved accuracy. Despite their advantages, VIO approaches introduce additional complexities, including sensor drift, calibration sensitivity, and increased computational cost.

Unlike these methods, SMF-VO directly estimates velocity using motion field equations from sparse optical flow, eliminating the need for explicit pose estimation via P3P algorithm or inertial sensing. By formulating the problem as a compact per-frame optimization, it reduces computational overhead enabling real-time operation on low-power embedded systems.

Ego-motion estimation with Motion Field. Motion field constraints have been widely studied in 3D computer vision [18], [19], describing the relationship between optical flow and camera motion in 3D. Based on this relationship, the motion field has been used to compute ground truth optical flow for LiDAR points in event camera datasets [20]–[23]. Recent studies have also explored their use in event-based vision, using high-speed asynchronous data to estimate motion. Self-supervised learning approaches [24], [25] first learn to estimate ego-motion and depth from event camera data and then utilize the motion field equation to compute optical flow. Shiba et al. [26] parameterized optical flow using motion field equations for contrast maximization in event cameras, while Lu et al. [27] fused motion field constraints with IMU data to recover velocity.

These methods, which either rely on event-based sensors or require IMU fusion, use the motion field equations to (1) apply them in parameterization processes for optimization, (2) estimate linear velocity only, or (3) estimate depth and ego motion jointly. In contrast, SMF-VO applies motion field constraints to standard RGB cameras to achieve direct egomotion estimation without the need for additional sensors or computationally expensive optimization.

Computational Efficiency in Visual Odometry. Efficient real-time VO is crucial for deployment in resource-constrained systems. Optimization-based SLAM frameworks such as ORB-SLAM3 [28] and Basalt [16] achieve high accuracy but require multi-threaded execution and substantial computational power. Lightweight VO systems such as SVO [8] and DSO [9] improve efficiency by reducing feature tracking overhead, but they still rely on photometric constraints, making them susceptible to lighting variations. SMF-VO achieves over 100 FPS speed without any GPU or hardware acceleration. This makes it a practical alternative for real-time applications on embedded platforms.

III. METHODOLOGY

The 3D motion of the camera can be computed from the motions of the projected points at known 3D positions [18], [19]. We briefly summarize the motion-field formulation below. The bold symbols represent vectors, and the subscript represents the corresponding coordinate in them, e.g., for $\mathbf{x} = [a \ b \ c]^{\top}$, $\mathbf{x}_x = a$, $\mathbf{x}_y = b$, and $\mathbf{x}_{(x,y)} = [a \ b]^{\top}$. The dot above a vector represents the temporal derivative of the vector, i.e. $\dot{\mathbf{x}} = \frac{d}{dt}\mathbf{x}$.

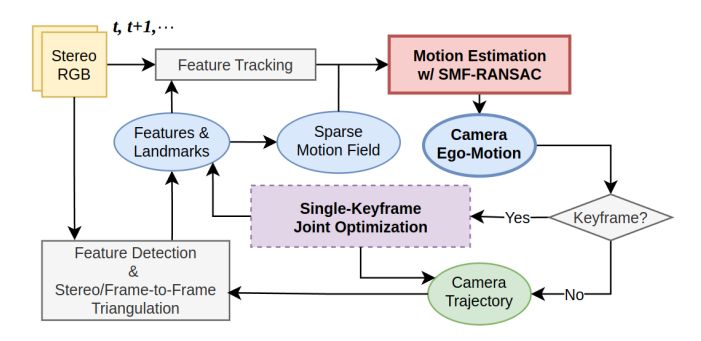


Fig. 2: Overview of the framework we propose.

A. 3D Camera Motion from Sparse Motion Field

For a 3D point in the camera coordinate frame, P = $[X \ Y \ Z]^{\top}$, the corresponding point projected onto the image plane at focal length f can be expressed as

$$\mathbf{p} = f \left(\mathbf{P}/Z \right) := [x \ y \ f]^{\top}. \tag{1}$$

When the camera moves with the linear velocity v and angular velocity ω , the movement (velocity) of the point P is described by

$$\dot{\mathbf{P}} = -\mathbf{v} - \boldsymbol{\omega} \times \mathbf{P}.\tag{2}$$

Differentiating both sides of (1) with respect to time gives

$$\dot{\mathbf{p}} = f(Z\dot{\mathbf{P}} - \dot{Z}\mathbf{P})/Z^2,\tag{3}$$

establishing the relationship between the velocity of the 3D point P and the velocity of p projected on the image plane. Substituting $\dot{\mathbf{P}}$ and \dot{Z} in (3) with (2), we obtain the following.

$$\dot{\mathbf{p}}_{x} = (\mathbf{v}_{z}x - \mathbf{v}_{x}f)/Z - \boldsymbol{\omega}_{y}f + \boldsymbol{\omega}_{z}y + (\boldsymbol{\omega}_{x}xy - \boldsymbol{\omega}_{y}x^{2})/f$$

$$\dot{\mathbf{p}}_{y} = (\mathbf{v}_{z}y - \mathbf{v}_{y}f)/Z - \boldsymbol{\omega}_{x}f + \boldsymbol{\omega}_{z}x + (\boldsymbol{\omega}_{y}xy - \boldsymbol{\omega}_{x}y^{2})/f$$
(4)

Let $\mathbf{u} = \dot{\mathbf{p}}_{(x,y)}$ be the pixel velocity at $\mathbf{p}_{(x,y)}$. From (4), we can obtain two constraints on the 3D camera motion s := $[\boldsymbol{\omega}^{\top} \mathbf{v}^{\top}]^{\top} \in \mathbb{R}^{6}$ from each pixel movement observed in the image,

$$\mathbf{u} = \begin{bmatrix} \mathbf{A}(\mathbf{p}) & \mathbf{B}(\mathbf{p})/Z \end{bmatrix} \mathbf{s}, \text{ where}$$
 (5)

$$\mathbf{A}(\mathbf{p}) = \begin{bmatrix} xy/f & -f - x^2/f & y \\ f + y^2/f & -xy/f & -x \end{bmatrix}, \mathbf{B}(\mathbf{p}) = \begin{bmatrix} -f & 0 & x \\ 0 & -f & y \end{bmatrix}$$

From n observed pixel velocities at the current frame, the 3D camera velocity can be estimated by solving the (overconstrained) linear system

$$\bar{\mathbf{u}} = \mathbf{W} \mathbf{s}, \text{ where}$$
 (6)

$$\bar{\mathbf{u}} = \mathbf{W} \mathbf{s}, \text{ where}$$

$$(6)$$

$$\bar{\mathbf{u}} = \begin{bmatrix} \mathbf{u}^1 \\ \mathbf{u}^2 \\ \vdots \\ \mathbf{u}^n \end{bmatrix} \in \mathbb{R}^{2n}, \mathbf{W} = \begin{bmatrix} \mathbf{A}(\mathbf{p}^1) & \mathbf{B}(\mathbf{p}^1)/Z^1 \\ \mathbf{A}(\mathbf{p}^2) & \mathbf{B}(\mathbf{p}^2)/Z^2 \\ \vdots & \vdots \\ \mathbf{A}(\mathbf{p}^n) & \mathbf{B}(\mathbf{p}^n)/Z^n \end{bmatrix} \in \mathbb{R}^{2n \times 6}.$$

The depth Z of each point in (6) can be obtained from the location of its corresponding landmark, which is estimated via stereo or frame-to-frame triangulation during motion estimation. For observations $n \geq 3$, we can solve the linear system above as

$$\hat{\mathbf{s}} = [\hat{\boldsymbol{\omega}}^{\top} \ \hat{\mathbf{v}}^{\top}]^{\top} = (\mathbf{W}^{\top} \mathbf{W})^{-1} \mathbf{W}^{\top} \bar{\mathbf{u}} .$$
 (7)

B. Motion Field with Normalized Ray

The 2D pixel-based motion field (Section III-A) is restricted to the ideal pinhole camera model, which prohibits its use with practical wide Field-of-View (FoV) systems like fisheye lenses. To address this, we derive a generalized 3D ray-based motion field equation operating on rays from the optical center, removing reliance on 2D pixel coordinates.

For a 3D point P in camera coordinate, the corresponding ray r can be expressed as

$$\mathbf{r} = \mathbf{P}/d := [x \ y \ z]^{\top}, \text{ where } d = ||\mathbf{P}||.$$
 (8)

Differentiating both sides of (8) with the same way of (1) to (3) gives

$$\dot{\mathbf{r}} = (d\dot{\mathbf{P}} - d\mathbf{P})/d^{2}, \text{ where } \dot{d} = (\mathbf{P} \cdot \dot{\mathbf{P}})/\|\mathbf{P}\| = \mathbf{r} \cdot \dot{\mathbf{P}},$$

$$\dot{\mathbf{r}} = \frac{d\dot{\mathbf{P}} - (\mathbf{r} \cdot \dot{\mathbf{P}})\mathbf{P}}{d^{2}} = \frac{d\dot{\mathbf{P}} - (\mathbf{P}\mathbf{r}^{\top})\dot{\mathbf{P}}}{d^{2}} = \frac{\mathbf{I} - \mathbf{r}\mathbf{r}^{\top}}{d}\dot{\mathbf{P}},$$
(9)

establishing the relationship between the velocity of the 3D point P and the flow (velocity) of corresponding ray r, that can be computed as $\dot{\mathbf{r}} = \mathbf{r}^{cur} - \mathbf{r}^{prev}$.

Substituting $\dot{\mathbf{P}}$ in (9) with (2), we obtain the following.

$$\dot{\mathbf{r}} = (\mathbf{I} - \mathbf{r}\mathbf{r}^{\top})(-\mathbf{v} - \boldsymbol{\omega} \times \mathbf{P})/d
= (\mathbf{I} - \mathbf{r}\mathbf{r}^{\top})[\mathbf{P}]_{\times} \boldsymbol{\omega}/d + (\mathbf{r}\mathbf{r}^{\top} - \mathbf{I})\mathbf{v}/d
= (\mathbf{I} - \mathbf{r}\mathbf{r}^{\top})[\mathbf{r}]_{\times} \boldsymbol{\omega} + (\mathbf{r}\mathbf{r}^{\top} - \mathbf{I})\mathbf{v}/d
= [\mathbf{r}]_{\times} \boldsymbol{\omega} + (\mathbf{r}\mathbf{r}^{\top} - \mathbf{I})\mathbf{v}/d$$
(10)

This derived equation is consistent with existing formulations in the literature, specifically matching the motion field equation for spherical projection presented in [29] under the condition f = 1. This validates that our general formulation yields an equivalent result for the special case of projection onto the unit sphere.

From (10), each ray movement provides three constraints on the 3D camera motion form each ray movement, $\dot{\mathbf{r}}_x, \dot{\mathbf{r}}_y, \dot{\mathbf{r}}_z$; however, these constraints are rank-deficient with an effective rank of two. Given n observed ray velocities at the current frame, the 3D camera velocity can be estimated by solving the resulting (over-constrained) linear system in the same manner as described in Section III-A.

$$\dot{\mathbf{u}} = \mathbf{M} \mathbf{s}, \text{ where}
\dot{\mathbf{u}} = [\dot{\mathbf{r}}^{1\top} \dot{\mathbf{r}}^{2\top} \dots \dot{\mathbf{r}}^{n\top}]^{\top} \in \mathbb{R}^{3n},
\mathbf{M} = \begin{bmatrix} [\mathbf{r}^{1}]_{\times} & (\mathbf{r}^{1}\mathbf{r}^{1\top} - \mathbf{I})/d^{1} \\ [\mathbf{r}^{2}]_{\times} & (\mathbf{r}^{2}\mathbf{r}^{2\top} - \mathbf{I})/d^{2} \\ \vdots & \vdots \\ [\mathbf{r}^{n}]_{\times} & (\mathbf{r}^{n}\mathbf{r}^{n\top} - \mathbf{I})/d^{n} \end{bmatrix} \in \mathbb{R}^{3n \times 6}$$
(11)

The Euclidean depth d of each point in (11) can be obtained by stereo depth estimation [30]. For observations $n \geq 3$, we can solve the linear system above as

$$\hat{\mathbf{s}} = \begin{bmatrix} \hat{\boldsymbol{\omega}}^\top & \hat{\mathbf{v}}^\top \end{bmatrix}^\top = \left(\mathbf{M}^\top \mathbf{M} \right)^{-1} \mathbf{M}^\top \hat{\mathbf{u}} . \tag{12}$$

Compared to the widely used P3P(PnP) algorithm [31] in visual odometry, our motion estimation method solves a simple 6×6 linear least squares problem of the form $\mathbf{A}\mathbf{x} = \mathbf{b}$ to compute the instantaneous camera motion $(\boldsymbol{\omega}, \mathbf{v})$. In contrast, the P3P algorithm requires solving a quartic polynomial to estimate the pose $[\mathbf{R}|\mathbf{t}]$, which is computationally heavier due to the need to disambiguate multiple solutions and perform backsubstitution.

C. Robust Estimation using RANSAC

In the previous section, we formulate the linear solver for 3D camera motion from pixel ray motions. However, the estimated pixel (ray) motions can be noisy or inconsistent due to outliers, e.g., independently moving objects. To handle such cases, the RANSAC algorithm [32] is commonly used, and we also use it for robust motion estimation, as in Alg 1.

Algorithm 1 Motion Field RANSAC Process

```
1: 
ightharpoonup \{ \mathbf{r}^i, \dot{\mathbf{r}}^i, d^i, \mathbf{P}_i \}_{i=1:n}: rays, flows, depths, landmarks
  2: \triangleright Q, n_s, N_{max}, \gamma_0, \tau_u, \tau_\theta: predefined parameters
  3: \triangleright \Theta(\mathbf{a}, \mathbf{b}): angle between two vectors \mathbf{a}, \mathbf{b} \in \mathbb{R}^3
  4: function ESTIMATE(\{j\})
               build M and \dot{\mathbf{u}} for the points in \{j\}.
                                                                                                         ⊳ eq (11)
  5:
               solve \hat{\mathbf{s}} for \hat{\mathbf{u}} = \mathbf{M}\hat{\mathbf{s}}. (\hat{\mathbf{s}} = [\hat{\boldsymbol{\omega}}^{\top}, \hat{\mathbf{v}}^{\top}]^{\top})
  6:
                                                                                                         ⊳ eq (12)
               for all i in 1:n do find the inliers \{i^*\} s.t.
  7:
                       \Theta\left((\mathbf{r}^i + \dot{\mathbf{r}}^i) , \operatorname{Exp}(\hat{\boldsymbol{\omega}})^\top (\mathbf{P}_i - \hat{\mathbf{v}})\right) < \tau_{\theta} \text{ and } 
||\dot{\mathbf{r}}^i - ([\mathbf{r}^i]_\times \hat{\boldsymbol{\omega}} + (\mathbf{r}^i \mathbf{r}^{i\top} - \mathbf{I}) \hat{\mathbf{v}}/d^i)|| < \tau_u 
  8:
  9:
10:
               return (\hat{\mathbf{s}}, \{i*\})
11: function RANSAC()
12:
               if n < n_s then return (0<sup>6</sup>, {})
               N_{iter} \leftarrow N_{max}, \ \mathbf{s}^* \leftarrow \mathbf{0}^6, \ I^* \leftarrow \{\}
13:
14:
                while #iteration < N_{iter} do
                       \{j\} \leftarrow n_s randomly selected indices in (1:n)
15:
                       (\mathbf{s}, I) \leftarrow \text{ESTIMATE}(\{j\})
16:
                       if ||I|| > ||I^*|| then
17:
                              \mathbf{s}^* \leftarrow \mathbf{s}, \ I^* \leftarrow I
18:
                              if ||I^*||/n > \gamma_0 then break while loop N_{iter} \leftarrow \min\left(\left\lceil \frac{\log(1-Q)}{\log(1-||I^*||/n)}\right\rceil, N_{iter}\right)
19:
20:
               if ||I^*|| > n_s then
21:
                       (\mathbf{s}, I) \leftarrow \text{ESTIMATE}(\{I^*\})
22:
                       if ||I|| > ||I^*|| then s^* \leftarrow s, I^* \leftarrow I
23:
               return (\mathbf{s}^*, I^*)
24:
```

In our framework, a set of ray velocities ù is estimated using Kanade-Lucas-Tomasi Feature Tracking [33] between consecutive frames.

The ESTIMATE() routine computes the linear least squares solution for a subset of ray motions and depths, while the RANSAC() routine iteratively refines 3D motion estimation by selecting the best model with the most inliers. The key RANSAC parameters are: success probability Q=99.99%, sample size $n_s=3$, early termination threshold $\gamma_0=0.9$, and inlier thresholds τ_u and τ_Π , that $\tau_u=2\sin(\tau_\Pi/2)$ for the ray-based, and $\tau_u=f\tan(\tau_\Pi)$ for the pixel-based motion field equation. To determine inliers from the instantaneous pixel ray motions, we evaluate the reprojection error and the motion residuals together.

Once the loop terminates, the final 3D camera motion and inliers are re-computed using all inliers, as the best motion from the RANSAC is initially derived from only n_s minimal data points. Contrary to the common belief that linearized formulations are suboptimal, we find that these solutions provide highly accurate camera trajectories even when simply accumulated over time. To further reduce the drift caused by real-world noise, as described in the next section, a simple non-linear optimization on the camera motion $(\hat{\omega}, \hat{\mathbf{v}})$ and landmark positions $\{P_i\}$ is applied.

D. Motion and Landmark Optimization

Although the 3D motion estimated by our SMF-RANSAC is generally accurate, small errors can accumulate over time, causing pose drift. Additionally, our algorithm uses landmark distances and depths from short-baseline stereo, which can be noisy, particularly for distant features. To address these issues, we incorporate a lightweight, bundle-adjustment-style, nonlinear optimization step. This process is optional, and even when used, it is highly efficient because it optimizes only the pose of the current keyframe and its associated landmarks while fixing the other keyframes. This approach is significantly more lightweight than conventional local bundle adjustment, which optimizes a much larger set of keyframes and landmarks.

Keyframes are selected following standard practices commonly used in graph-based VO/SLAM systems. Specifically, a frame is promoted to a keyframe when the number of tracked inlier features falls below a threshold ($<\tau_n$, where τ_n denotes the desired minimum number of observed features), or based on the elapsed time and the magnitude of relative motion between the current frame and the last keyframe, quantified by $||\mathbf{R}||$ and $||\mathbf{t}||$.

If a frame is selected as a keyframe, a lightweight nonlinear optimization is performed to refine the motion estimate and the landmark positions as

$$\{[\mathbf{R}|\mathbf{t}]^{k}\}, \{\mathbf{P}_{l}\} = \underset{\{[\mathbf{R}|\mathbf{t}]^{k}\}, \{\mathbf{P}_{l}\}}{\operatorname{argmin}} \sum_{k,l} \rho \left(\left\| \mathbf{r}_{l}^{k} - \frac{\mathbf{R}^{k^{\top}}(\mathbf{P}_{l} - \mathbf{t}^{k})}{\left\| \mathbf{R}^{k^{\top}}(\mathbf{P}_{l} - \mathbf{t}^{k}) \right\|} \right\| \right).$$
(13)

All inlier landmarks \mathbf{P}_l observed in the newly selected keyframe, along with the poses of the keyframes $[\mathbf{R}|\mathbf{t}]^k$ that observe these landmarks, are jointly optimized by minimizing the reprojection ray errors between the observed and predicted rays. In our approach, only the pose of the newly selected keyframe is treated as active, while all other keyframe poses remain fixed. This design keeps the problem size small, enabling efficient optimization and maintaining high-speed execution. The robust Cauchy loss function is applied, defined as $\rho(s) = c^2 \cdot \log \left(1 + s/c^2\right)$, where c is a tunable scale parameter.

This procedure resembles typical bundle adjustment but is restricted to only the landmarks observed in the current keyframe. Consequently, it is significantly more lightweight than conventional local bundle adjustment, enabling high-speed execution even on embedded platforms such as the Raspberry Pi.

RMSE ATE (m)	Method	Avg	MH01	MH02	MH03	MH04	MH05	V101	V102	V103	V201	V202
SMF-VO (ours)	stereo VO	0.128	0.099	0.039	0.169	0.208	0.348	0.063	0.100	0.088	0.057	0.114
BASALT [34]	stereo VO	0.333	0.072	0.082	0.116	0.176	0.152	0.058	0.124	1.974	0.068	0.511
*ORB-SLAM3 [28]	stereo VO	0.088	0.048	0.017	0.033	0.103	0.181	0.036	0.073	0.260	0.042	0.088
VINS-FUSION [15]	stereo VO	0.731	0.511	0.598	0.468	0.850	0.611	0.555	0.733	2.502	0.256	0.224
OKVIS2 [17]	stereo VO	0.115	0.070	0.115	0.111	0.251	0.124	0.071	0.084	0.206	0.047	0.071
BASALT [16]	stereo VIO	0.068	0.065	0.062	0.062	0.114	0.145	0.043	0.045	0.054	0.039	0.049
*ORB-SLAM3 [28]	stereo VIO	0.037	0.043	0.038	0.104	0.110	0.087	0.144	0.474	0.066	0.103	0.121
VINS-FUSION [15]	stereo VIO	0.213	0.267	0.223	0.306	0.441	0.314	0.112	0.101	0.114	0.126	0.121
OKVIS2 [17]	stereo VIO	0.063	0.072	0.054	0.108	0.102	0.090	0.054	0.053	0.030	0.043	0.026
OpenVINS [35]	stereo VIO	0.144	0.084	0.095	0.165	0.295	0.517	0.061	0.055	0.056	0.062	0.052
SchurVINS [14]	stereo VIO	0.086	0.076	0.067	0.097	0.183	0.138	0.048	0.051	0.083	0.036	0.078
*ROVIO [13]	mono VIO	0.433	0.267	fail	0.383	0.785	1.289	0.165	0.182	0.192	0.243	0.393
milliseconds/frame	Method	Avg	MH01	MH02	MH03	MH04	MH05	V101	V102	V103	V201	V202
OR 500 0 1												
SMF-VO (ours)	stereo VO	7.789	5.419	5.949	7.344	8.317	8.041	6.088	9.355	10.839	6.096	10.443
BASALT [16]	stereo VO stereo VO	7.789 23.706	5.419 29.101	5.949 27.447	7.344 28.231	8.317 26.690	8.041 25.990	6.088 23.980	9.355 20.473	10.839 16.482	6.096 20.597	18.065
BASALT [16]	stereo VO	23.706	29.101	27.447	28.231	26.690	25.990	23.980	20.473	16.482	20.597	18.065
BASALT [16] *ORB-SLAM3 [28]	stereo VO stereo VO	23.706 65.674	29.101 83.890	$\frac{27.447}{72.340}$	$\frac{28.231}{72.568}$	26.690 64.944	25.990 67.565	$\frac{23.980}{61.035}$	$\frac{20.473}{55.170}$	$\frac{16.482}{52.934}$	20.597 54.699	$\frac{18.065}{71.585}$
BASALT [16] *ORB-SLAM3 [28] VINS-FUSION [15]	stereo VO stereo VO	23.706 65.674 51.506	29.101 83.890 51.304	27.447 72.340 51.023	28.231 72.568 50.799	26.690 64.944 51.070	25.990 67.565 51.062	23.980 61.035 51.007	20.473 55.170 55.836	16.482 52.934 51.817	20.597 54.699 50.560	18.065 71.585 50.583
BASALT [16] *ORB-SLAM3 [28] VINS-FUSION [15] OKVIS2 [17]	stereo VO stereo VO stereo VO stereo VO	23.706 65.674 51.506 127.902	29.101 83.890 51.304 167.920	27.447 72.340 51.023 161.468	28.231 72.568 50.799 157.856	26.690 64.944 51.070 129.044	25.990 67.565 51.062 132.349	23.980 61.035 51.007 121.978	20.473 55.170 55.836 105.822	16.482 52.934 51.817 86.944	20.597 54.699 50.560 111.945	18.065 71.585 50.583 103.690
BASALT [16] *ORB-SLAM3 [28] VINS-FUSION [15] OKVIS2 [17] BASALT [16]	stereo VO stereo VO stereo VO stereo VIO	23.706 65.674 51.506 127.902 20.032	29.101 83.890 51.304 167.920 23.199	27.447 72.340 51.023 161.468 23.146	28.231 72.568 50.799 157.856 22.403	26.690 64.944 51.070 129.044 21.743	25.990 67.565 51.062 132.349 22.169	23.980 61.035 51.007 121.978 20.961	20.473 55.170 55.836 105.822 17.201	16.482 52.934 51.817 86.944 13.770	20.597 54.699 50.560 111.945 19.315	18.065 71.585 50.583 103.690 16.414
BASALT [16] *ORB-SLAM3 [28] VINS-FUSION [15] OKVIS2 [17] BASALT [16] *ORB-SLAM3 [28]	stereo VO stereo VO stereo VO stereo VIO stereo VIO	23.706 65.674 51.506 127.902 20.032 65.467	29.101 83.890 51.304 167.920 23.199 76.937	27.447 72.340 51.023 161.468 23.146 77.294	28.231 72.568 50.799 157.856 22.403 82.313	26.690 64.944 51.070 129.044 21.743 64.680	25.990 67.565 51.062 132.349 22.169 67.881	23.980 61.035 51.007 121.978 20.961 57.988	20.473 55.170 55.836 105.822 17.201 53.220	16.482 52.934 51.817 86.944 13.770 52.451	20.597 54.699 50.560 111.945 19.315 53.848	18.065 71.585 50.583 103.690 16.414 68.059
BASALT [16] *ORB-SLAM3 [28] VINS-FUSION [15] OKVIS2 [17] BASALT [16] *ORB-SLAM3 [28] VINS-FUSION [15]	stereo VO stereo VO stereo VO stereo VIO stereo VIO stereo VIO	23.706 65.674 51.506 127.902 20.032 65.467 51.506	29.101 83.890 51.304 167.920 23.199 76.937 51.366	27.447 72.340 51.023 161.468 23.146 77.294 51.055	28.231 72.568 50.799 157.856 22.403 82.313 50.815	26.690 64.944 51.070 129.044 21.743 64.680 51.100	25.990 67.565 51.062 132.349 22.169 67.881 51.046	23.980 61.035 51.007 121.978 20.961 57.988 51.003	20.473 55.170 55.836 105.822 17.201 53.220 55.785 108.578 68.862	16.482 52.934 51.817 86.944 13.770 52.451 51.741	20.597 54.699 50.560 111.945 19.315 53.848 50.591	18.065 71.585 50.583 103.690 16.414 68.059 50.561
BASALT [16] *ORB-SLAM3 [28] VINS-FUSION [15] OKVIS2 [17] BASALT [16] *ORB-SLAM3 [28] VINS-FUSION [15] OKVIS2 [17]	stereo VO stereo VO stereo VO stereo VIO stereo VIO stereo VIO stereo VIO	23.706 65.674 51.506 127.902 20.032 65.467 51.506 128.576	29.101 83.890 51.304 167.920 23.199 76.937 51.366 173.060	27.447 72.340 51.023 161.468 23.146 77.294 51.055 163.651	28.231 72.568 50.799 157.856 22.403 82.313 50.815 157.079	26.690 64.944 51.070 129.044 21.743 64.680 51.100 124.421	25.990 67.565 51.062 132.349 22.169 67.881 51.046 127.595	23.980 61.035 51.007 121.978 20.961 57.988 51.003 124.556	20.473 55.170 55.836 105.822 17.201 53.220 55.785 108.578	16.482 52.934 51.817 86.944 13.770 52.451 51.741 86.777	20.597 54.699 50.560 111.945 19.315 53.848 50.591 113.889	18.065 71.585 50.583 103.690 16.414 68.059 50.561 106.154

TABLE I: **RMSE ATE** (m) and execution time (ms/frame) on the EuRoC dataset using a Raspberry Pi 5 (2.4 GHz quadcore). The V203 sequence contains many featureless frames, causing failures in most odometry systems, and is therefore excluded. Refer to the text for the details on ROVIO and ORB-SLAM3. The best result is shown in **bold**, and the second-best is <u>underlined</u>. Entries marked "fail" indicate RMSE ATE values exceeding 100 m. Our system achieves the fastest average speed and can operate at 100 Hz on lightweight embedded platforms.

RMSE ATE (m)	Method	Avg	00	02	03	04	05	06	07	08	09	10
SMF-VO (ours)	stereo VO	2.886	3.833	5.604	1.519	1.561	2.490	3.568	1.346	3.557	4.313	1.074
BASALT [16]	stereo VO	3.267	3.864	10.594	1.330	1.289	2.930	2.532	1.403	3.766	3.845	1.114
*ORB-SLAM3 [28]	stereo VO	2.668	4.811	8.122	0.776	0.218	1.840	1.834	1.383	3.558	3.078	1.062
VINS-FUSION [15]	stereo VO	7.241	12.295	22.353	1.862	1.553	6.189	3.838	2.210	10.388	8.125	3.601
milliseconds/frame	36.43.3											
miniseconus/ii ame	Method	Avg	00	02	03	04	05	06	07	08	09	10
SMF-VO (ours)	stereo VO	Avg 19.348	00 19.411	21.469	13.874	21.169	05 19.691	06 21,214	07 16.818	19.382	21.937	10 18.513
		0									*-	
SMF-VO (ours)	stereo VO	19.348	19.411	21.469	13.874	21.169	19.691	21.214	16.818	19.382	21.937	18.513

TABLE II: **RMSE ATE** (m) and execution time (ms/frame) on the KITTI dataset using a Raspberry Pi 5 (2.4 GHz quad-core). The 01 sequence contains many featureless frames and dynamic objects, causing failures in most odometry systems, and is therefore excluded. Refer to the text for the details on ORB-SLAM3. The best result is shown in **bold**, and the second-best is underlined.

			RMSE ATE (m)						milliseconds/frame						
	Method	Avg	R1	R2	R3	R4	R5	R6	Avg	R1	R2	R3	R4	R5	R6
SMF-VO (ours)	stereo VO	0.082	0.053	0.183	0.114	0.036	0.059	0.048	9.733	11.501	8.551	8.231	10.077	11.201	8.836
BASALT [16]	stereo VO	0.205	0.112	0.128	0.157	0.039	0.758	0.034	14.342	14.374	13.756	13.542	14.690	13.489	16.200
*ORB-SLAM3 [28]	stereo VO	0.079	0.078	0.052	0.099	0.082	0.077	0.086	79.965	77.761	77.387	78.585	85.519	82.275	78.264
OKVIS2 [17]	stereo VO	0.104	0.085	0.134	0.169	0.021	0.142	0.070	94.768	97.108	94.894	93.885	91.408	96.467	94.845
BASALT [16]	stereo VIO	0.095	0.108	0.076	0.133	0.052	0.180	0.020	19.344	19.235	18.581	17.404	20.501	17.317	23.024
*ORB-SLAM3 [28]	stereo VIO	0.044	0.038	0.102	0.059	0.010	0.011	0.043	72.636	70.178	73.244	71.614	72.932	74.797	73.051
OKVIS2 [17]	stereo VIO	0.067	0.054	0.124	0.099	0.042	0.038	0.048	91.096	95.178	91.234	90.934	86.515	90.585	92.129
OpenVINS [35]	stereo VIO	0.081	0.072	0.139	0.106	0.030	0.079	0.057	43.083	41.156	40.382	41.687	51.948	41.465	41.862

TABLE III: **RMSE ATE(m)** and **Execution time (ms/frame)** on the **TUM-VI Room dataset** using a Raspberry Pi 5 (2.4 GHz quad-core). Refer to the text for the details on ORB-SLAM3. The best value is shown in **bold**, and the second best is underlined.

IV. EXPERIMENTAL EVALUATION

We evaluate the proposed visual odometry method on three benchmark datasets: EuRoC [36], KITTI [37], and TUM-VI [38]. The EuRoC dataset, collected with a micro aerial vehicle, provides 11 stereo–IMU sequences. KITTI, a standard benchmark for autonomous driving, offers 11

car-mounted sequences with GPS/INS ground truth. TUM-VI contains fisheye stereo and IMU data under challenging motion; we use the Room sequences, as they are the only ones with full ground truth trajectories.

We compare our method against state-of-the-art VO/VIO algorithms under identical conditions. All experiments run on

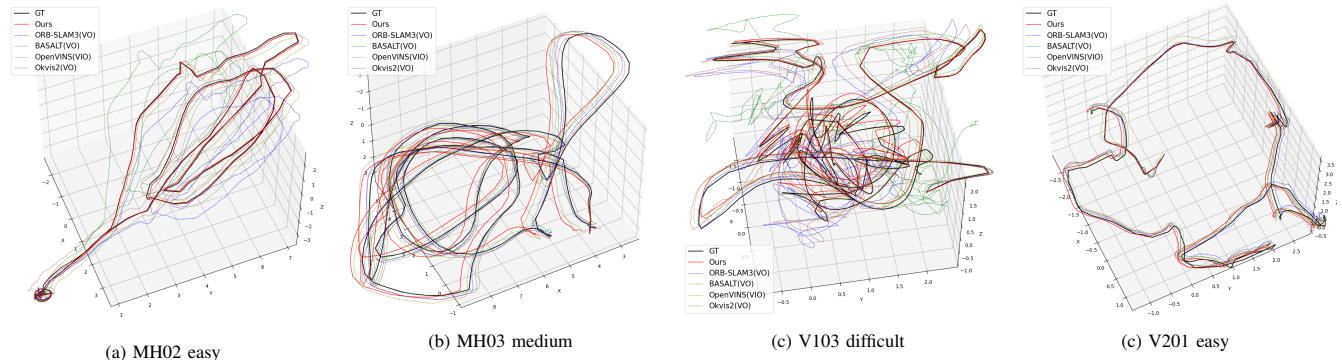
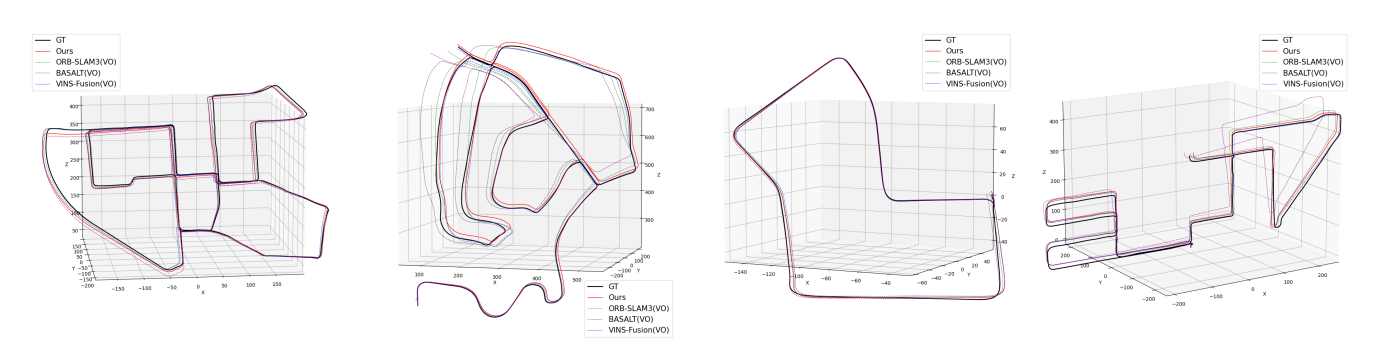


Fig. 3: Qualitative trajectory result of EuRoC sequences. The estimated trajectories of SMF-VO (ours), ORB-SLAM3 [28] (VO), Basalt [16] (VO), OpenVINS [35] (VIO), and OKVIS2 [17] (VO) are aligned to the ground truth pose at the first frame.



(a) kitti 00 (b) kitti 02 (c) kitti 07 (c) kitti 08 (E) Fig. 4: Qualitative trajectory result of KITTI sequences. The estimated trajectories of SMF-VO (ours), ORB-SLAM3 [28] (VO), Basalt [16] (VO), and VINS-Fusion [15] (VO) are aligned to the ground truth pose at the first frame.

a Raspberry Pi 5 (2.4 GHz quad-core ARM CPU) without GPU or hardware acceleration. Each baseline is tested both in our setting (stereo without IMU) and in its recommended configuration (e.g., monocular or with IMU). For ROVIO, only filter update time is measured. For ORB-SLAM3, we report tracking time excluding image preprocessing, which may make runtimes appear slightly faster.

Performance metrics are:

- Accuracy: RMSE of Absolute Trajectory Error (ATE).
- Efficiency: Execution time on Raspberry Pi.

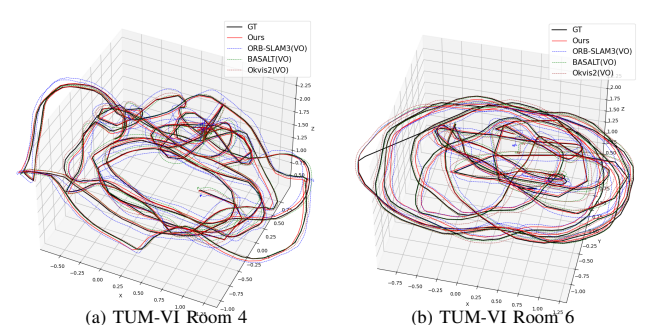


Fig. 5: Qualitative trajectory results for TUM-VI Room sequences. The estimated trajectories of SMF-VO (ours), ORB-SLAM3 [28] (VO), Basalt [16] (VO), and OKVIS2 [17] (VO) are aligned to the ground truth pose at the first frame.

Finally, we conduct an ablation study to analyze the contribution of each component in the proposed SMF-VO framework.

A. Evaluation on Benchmark Datasets

Tables I, II, and III report trajectory accuracy (RMSE ATE) and per-frame processing time for the EuRoC, KITTI, and TUM-VI Room datasets, emphasizing the efficiency of our method. For VO-only evaluation, loop closure is disabled in systems that provide it (e.g., ORB-SLAM3, VINS-FUSION, SchurVINS etc.). Qualitative trajectories are shown in Fig. 3, 4, and 5, illustrating the robustness of our method against baselines and ground truth.

a) EuRoC: On EuRoC (Table I), ORB-SLAM3 achieves the best VO-only accuracy with centimeter-level errors, benefiting from global bundle adjustment. Our method attains accuracy comparable to ORB-SLAM3, OKVIS2, and BASALT, with BASALT slightly ahead on some sequences due to local refinement. On average, SMF-VO ranks third, with an average error of approximately 0.1m.

In efficiency, ORB-SLAM3 and OKVIS2 require 65~128 ms/frame on average, while SMF-VO runs in under 10 ms/frame, supporting operation at over 100 Hz on embedded boards. With IMU integration (VIO), only ORB-SLAM3, OKVIS2, and BASALT surpass SMF-VO in accuracy. BASALT particularly benefits from IMU data on challenging sequences such as V103.

	w/o no	onlinear op	timizatio	n III-D	w/ no	nlinear op	timization	III-D
	pixel-ba	sed III-A	ray-bas	sed III-B	pixel-bas	sed III-A	ray-bas	ed III-B
	ms/f	RMSE	ms/f	RMSE	ms/f	RMSE	ms/f	RMSE
MH01	4.838	0.318	5.049	0.240	5.281	0.075	5.419	0.099
MH02	5.030	0.287	4.957	0.214	5.955	0.099	5.949	0.039
MH03	4.914	1.070	4.987	0.783	7.285	0.173	7.344	0.169
MH04	5.092	5.491	5.052	5.722	8.948	0.297	8.317	0.208
MH05	4.784	3.277	5.090	3.386	7.889	0.267	8.041	0.348
V101	4.914	0.235	4.840	0.187	5.986	0.083	6.088	0.063
V102	4.993	0.382	4.900	0.396	9.394	0.123	9.355	0.100
V103	5.026	0.644	4.916	0.628	11.322	0.097	10.839	0.088
V201	4.818	0.184	4.854	0.281	6.045	0.064	6.096	0.057
V202	5.166	0.511	4.966	0.186	10.344	0.125	10.443	0.114
Avg	4.957	1.240	4.961	1.202	7.845	0.140	7.789	0.128
Room1	4.236	4.339	3.805	0.897	10.897	0.111	11.501	0.053
Room2	3.866	1.916	3.840	1.212	9.147	0.209	8.551	0.183
Room3	4.414	1.505	3.819	1.089	9.719	0.136	8.231	0.114
Room4	3.919	1.261	3.780	0.251	9.741	0.041	10.077	0.036
Room5	4.475	4.823	3.997	0.754	10.770	0.103	11.201	0.059
Room6	3.658	0.631	3.753	0.320	8.725	0.051	8.836	0.048
Avg	4.095	2.413	3.832	0.754	9.833	0.108	9.733	0.082

TABLE IV: Ablation studies were performed on pixel-based and ray-based motion field algorithms, both with and without the proposed lightweight nonlinear optimization step. The values with better accuracy (RMSE ATE (m)) in each setup (w/ and w/o nonlinear optimization) are shown in **bold**. The results highlight the benefits of the proposed ray-based approach and the effectiveness of the lightweight nonlinear optimization.

b) KITTI: On KITTI (Table II), which provides only stereo images, ORB-SLAM3 again achieves the highest accuracy. Our method delivers similar accuracy with the lowest execution time. Compared to BASALT, the second-fastest VO system, SMF-VO is both more accurate and faster. Despite KITTI's higher resolution and lower frame rate, our method processes frames in under 20 ms, ensuring real-time operation while remaining fast and efficient enough for deployment on embedded devices. These results confirm that SMF-VO generalizes well from small-scale indoor to large-scale outdoor environments, maintaining a favorable balance between accuracy and efficiency.

c) TUM-VI Room: On TUM-VI Room (Table III), which includes fisheye stereo, IMU, and ground-truth trajectories from motion capture, ORB-SLAM3 achieves the highest VO-only accuracy with centimeter-level errors. SMF-VO attains comparable accuracy, slightly surpassing ORB-SLAM3 on some sequences, and ranks second overall with an average error of about 0.08 m. In terms of efficiency, SMF-VO operates roughly 8× faster than ORB-SLAM3 and 1.5× faster than BASALT. Compared to VIO methods, SMF-VO remains highly competitive: it delivers higher accuracy than BASALT while requiring substantially less computation than the most accurate IMU-based systems, making it particularly attractive for embedded platforms.

B. Ablation

Ablation studies were conducted to compare the performance of the ray-based motion field (Section III-B) with the conventional pixel-based motion field (Section III-A), and to determine the effect of adding a lightweight nonlinear optimization step after RANSAC-based motion estimation.

As shown in Table IV, the 3D ray-based formulation consistently improves trajectory accuracy, particularly on

wide field-of-view data such as the TUM-VI Room sequences. The performance gap becomes more pronounced when nonlinear optimization is omitted. This is because, in the 2D pixel-based formulation, the error bound on pixel locations grows with distance from the image center, making the linear system $\mathbf{A}\mathbf{x} = \mathbf{b}$ less reliable and more sensitive to outliers. In contrast, the 3D ray-based formulation maintains a consistent angular error metric—measuring deviations in degrees between observed and reprojected rays—regardless of image distortion or projection model. This property makes it more robust and better suited to wide FoV or distorted cameras, whereas the 2D pixel-based method assumes an ideal pinhole model.

Regarding runtime, omitting the nonlinear optimization step reduces computation further, while maintaining acceptable accuracy on sequences with simple motion and sufficient texture (e.g., MH01, MH02, V101, V201). Although the optimization step significantly improves accuracy in challenging cases, in structured and less dynamic environments it can be skipped to achieve faster execution with only a modest loss in accuracy.

V. CONCLUSION

In this paper, we introduce SMF-VO, a novel motion-centric visual odometry framework that directly estimates ego-motion from sparse optical flow using the motion field equation. Unlike conventional VO methods that rely on explicit pose estimation and computationally expensive map optimization, SMF-VO computes instantaneous linear and angular velocities from a sparse motion field using a highly efficient linear solution, complemented by an optional, lightweight nonlinear refinement step.

Through extensive experiments on standard benchmark datasets, we demonstrated that SMF-VO significantly outperforms conventional VO approaches in computational efficiency while maintaining competitive accuracy. Our algorithm achieved over 100 FPS on a Raspberry Pi 5 using only a CPU, highlighting its suitability for real-time applications on low-power embedded platforms.

In conclusion, SMF-VO establishes a new, motion-centric state estimation paradigm that offers a scalable and efficient alternative to conventional VO. Its exceptional computational efficiency makes it a strong candidate for practical, real-world applications in mobile robotics, AR/VR, and wearable devices. Future work will explore its application to diverse sensor modalities, including event cameras and IMU fusion.

REFERENCES

- A. J. Davison, "Real-time simultaneous localisation and mapping with a single camera," in *Proceedings of the Ninth IEEE International Conference on Computer Vision (ICCV)*, vol. 2. IEEE, October 2003, pp. 1403–1410.
- [2] E. Mouragnon, M. Lhuillier, M. Dhome, F. Dekeyser, and P. Sayd, "Real-time localization and 3d reconstruction," in *Proceedings of the* 2006 IEEE Computer Society Conference on Computer Vision and Pattern Recognition (CVPR'06), vol. 1. IEEE, June 2006, pp. 363– 370.
- [3] G. Klein and D. Murray, "Parallel tracking and mapping for small ar workspaces," in *Proceedings of the 6th IEEE and ACM International Symposium on Mixed and Augmented Reality (ISMAR)*. IEEE, November 2007, pp. 225–234.

- [4] R. Mur-Artal, J. M. M. Montiel, and J. D. Tardos, "Orb-slam: A versatile and accurate monocular slam system," *IEEE Transactions* on Robotics, vol. 31, no. 5, pp. 1147–1163, 2015.
- [5] A. Geiger, J. Ziegler, and C. Stiller, "Stereoscan: Dense 3d reconstruction in real-time," in *Proceedings of the 2011 IEEE Intelligent Vehicles Symposium (IV)*. IEEE, June 2011, pp. 963–968.
- [6] R. Mur-Artal and J. D. Tardós, "Orb-slam2: An open-source slam system for monocular, stereo, and rgb-d cameras," *IEEE Transactions* on Robotics, vol. 33, no. 5, pp. 1255–1262, 2017.
- [7] J. Engel, T. Schöps, and D. Cremers, "Lsd-slam: Large-scale direct monocular slam," in ECCV. Springer International Publishing, September 2014, pp. 834–849.
- [8] C. Forster, Z. Zhang, M. Gassner, M. Werlberger, and D. Scaramuzza, "Svo: Semidirect visual odometry for monocular and multicamera systems," *IEEE Transactions on Robotics*, vol. 33, no. 2, pp. 249– 265, 2016.
- [9] J. Engel, V. Koltun, and D. Cremers, "Direct sparse odometry," *IEEE TPAMI*, vol. 40, no. 3, pp. 611–625, 2017.
- [10] H. Strasdat, A. J. Davison, J. M. Montiel, and K. Konolige, "Double window optimisation for constant time visual slam," in *Proceedings* of the 2011 International Conference on Computer Vision (ICCV). IEEE, November 2011, pp. 2352–2359.
- [11] R. Kümmerle, G. Grisetti, H. Strasdat, K. Konolige, and W. Burgard, "g2o: A general framework for graph optimization," in *Proceedings of the 2011 IEEE International Conference on Robotics and Automation (ICRA)*. IEEE, May 2011, pp. 3607–3613.
- [12] A. I. Mourikis and S. I. Roumeliotis, "A multi-state constraint kalman filter for vision-aided inertial navigation," in *IEEE International Con*ference on Robotics and Automation. IEEE, April 2007, pp. 3565– 3572.
- [13] M. Bloesch, M. Burri, S. Omari, M. Hutter, and R. Siegwart, "Iterated extended kalman filter based visual-inertial odometry using direct photometric feedback," *The International Journal of Robotics Research*, vol. 36, no. 10, pp. 1053–1072, 2017.
- [14] Y. Fan, T. Zhao, and G. Wang, "Schurvins: Schur complement-based lightweight visual inertial navigation system," in *Proceedings of the IEEE/CVF Conference on Computer Vision and Pattern Recognition* (CVPR), June 2024, pp. 17964–17973.
- [15] T. Qin, P. Li, and S. Shen, "Vins-mono: A robust and versatile monocular visual-inertial state estimator," *IEEE Transactions on Robotics*, vol. 34, no. 4, pp. 1004–1020, 2018.
- [16] V. Usenko, N. Demmel, D. Schubert, J. Stückler, and D. Cremers, "Visual-inertial mapping with non-linear factor recovery," *IEEE Robotics and Automation Letters*, vol. 5, no. 2, pp. 422–429, 2019.
- [17] S. Leutenegger, "Okvis2: Realtime scalable visual-inertial slam with loop closure," arXiv preprint arXiv:2202.09199, 2022. [Online]. Available: https://arxiv.org/abs/2202.09199
- [18] H. C. Longuet-Higgins and K. Prazdny, "The interpretation of a moving retinal image," *Proceedings of the Royal Society of London. Series B. Biological Sciences*, vol. 208, no. 1173, pp. 385–397, 1980. [Online]. Available: https://royalsocietypublishing.org/doi/abs/ 10.1098/rspb.1980.0057
- [19] E. Trucco and A. Verri, Introductory Techniques for 3-D Computer Vision. Englewood Cliffs: Prentice Hall, 1998, vol. 201.
- [20] A. Z. Zhu, D. Thakur, T. Özaslan, B. Pfrommer, V. Kumar, and K. Daniilidis, "The multivehicle stereo event camera dataset: An event camera dataset for 3d perception," *IEEE Robotics and Automation Letters*, vol. 3, no. 3, pp. 2032–2039, 2018.
- [21] A. Z. Zhu, L. Yuan, K. Chaney, and K. Daniilidis, "Ev-flownet: Self-supervised optical flow estimation for event-based cameras," in Proceedings of Robotics: Science and Systems (RSS), Pittsburgh, Pennsylvania, June 2018.

- [22] M. Gehrig, W. Aarents, D. Gehrig, and D. Scaramuzza, "Dsec: A stereo event camera dataset for driving scenarios," *IEEE Robotics and Automation Letters*, vol. 6, no. 3, pp. 4947–4954, 2021.
- [23] M. Gehrig, M. Millhäusler, D. Gehrig, and D. Scaramuzza, "E-raft: Dense optical flow from event cameras," in *Proceedings of the 2021 International Conference on 3D Vision (3DV)*. IEEE, December 2021, pp. 197–206.
- [24] A. Z. Zhu, L. Yuan, K. Chaney, and K. Daniilidis, "Unsupervised event-based learning of optical flow, depth, and egomotion," in CVPR. IEEE, 2019, pp. 989–997.
- [25] C. Ye, A. Mitrokhin, C. Fermüller, J. A. Yorke, and Y. Aloimonos, "Unsupervised learning of dense optical flow, depth and egomotion with event-based sensors," in *IEEE/RSJ International Conference on Intelligent Robots and Systems*. IEEE, October 2020, pp. 5831–5838.
- [26] S. Shiba, Y. Klose, Y. Aoki, and G. Gallego, "Secrets of event-based optical flow, depth and ego-motion estimation by contrast maximization," *IEEE TPAMI*, 2024.
- [27] X. Lu, Y. Zhou, J. Niu, S. Zhong, and S. Shen, "Event-based visual inertial velometer," in *Proceedings of Robotics: Science and Systems (RSS)*. Delft, Netherlands: CKS Robotic Institute, Hong Kong University of Science and Technology and School of Robotics, Hunan University, July 2024, equal contribution by Xiuyuan Lu and Yi Zhou.
- [28] C. Campos, R. Elvira, J. J. G. Rodríguez, J. M. Montiel, and J. D. Tardós, "Orb-slam3: An accurate open-source library for visual, visual-inertial, and multimap slam," *IEEE Transactions on Robotics*, vol. 37, no. 6, pp. 1874–1890, 2021.
- [29] T.-W. Hui and R. Chung, "Determining motion directly from normal flows upon the use of a spherical eye platform," in *Proceedings of the IEEE Conference on Computer Vision and Pattern Recognition*, 2013, pp. 2267–2274.
- [30] R. Hartley and A. Zisserman, Multiple View Geometry in Computer Vision. Cambridge University Press, 2003.
- [31] X.-S. Gao, X.-R. Hou, J. Tang, and H.-F. Cheng, "Complete solution classification for the perspective-three-point problem," *IEEE TPAMI*, vol. 25, no. 8, pp. 930–943, August 2003.
- [32] M. A. Fischler and R. C. Bolles, "Random sample consensus: A paradigm for model fitting with applications to image analysis and automated cartography," *Communications of the ACM*, vol. 24, no. 6, pp. 381–395, 1981.
- [33] S. Baker and I. Matthews, "Lucas-kanade 20 years on: A unifying framework," *International Journal of Computer Vision*, vol. 56, pp. 221–255, 2004.
- [34] L. V. Stumberg, V. Usenko, and D. Cremers, "Direct sparse visual-inertial odometry using dynamic marginalization," in *IEEE International Conference on Robotics and Automation*. IEEE, May 2018, pp. 2510–2517.
- [35] P. Geneva, K. Eckenhoff, W. Lee, Y. Yang, and G. Huang, "Openvins: A research platform for visual-inertial estimation," in *IEEE International Conference on Robotics and Automation*. IEEE, May 2020, pp. 4666–4672.
- [36] M. Burri, J. Nikolic, P. Gohl, T. Schneider, J. Rehder, S. Omari, M. W. Achtelik, and R. Siegwart, "The euroc micro aerial vehicle datasets," *The International Journal of Robotics Research*, vol. 35, no. 10, pp. 1157–1163, 2016.
- [37] A. Geiger, P. Lenz, and R. Urtasun, "Are we ready for autonomous driving? the kitti vision benchmark suite," in CVPR. Providence, RI, USA: IEEE, June 2012, pp. 3354–3361.
- [38] D. Schubert, T. Goll, N. Demmel, V. Usenko, J. Stückler, and D. Cremers, "The tum vi benchmark for evaluating visual-inertial odometry," in *IEEE/RSJ International Conference on Intelligent Robots and Systems*. Madrid, Spain: IEEE, October 2018, pp. 1680–1687.